

Experimental Validation of Phase Velocity and Interaction Impedance of Meander Line Slow Wave Structures for Space Traveling Wave Tubes

Juan M. Socuéllamos, Roberto Dionisio, Rosa Letizia, *Senior Member, IEEE*, and Claudio Paoloni, *Senior Member, IEEE*

Abstract—Meander lines are promising slow wave structures (SWSs) for millimeter-wave traveling wave tubes (TWTs) due to low-cost manufacture, low-voltage operation and high interaction impedance. However, experimental results on meander lines are rare in literature.

Phase velocity and interaction impedance are the most important parameters for the design and characterization of TWT SWSs. Their experimental determination in meander lines is crucial for validating simulations and developing new topologies.

Based on a new theoretical model, this paper presents an experimental procedure to determine the phase velocity and the interaction impedance. The method is validated on four different Ka-band (33-37 GHz) meander line SWSs, including two of a novel topology.

Index Terms—Interaction impedance, meander line, millimeter wave, phase velocity, satellite communications, slow wave structure (SWS), traveling wave tube (TWT)

I. INTRODUCTION

THE exploitation of the millimeter wave spectrum for satellite communications is growing in interest due to the wide frequency bands available and the short wavelength that permits to reduce size and weight of payload. In particular, the Ka-band (26.5-40 GHz) is opening new perspectives for High Throughput Satellites (HTS) to be integrated in the new 5G networks [1], [2]. Traveling wave tubes (TWTs) are the only devices capable of providing high power over a wide frequency band to enable satellite internet distribution at millimeter waves [3]. Microwave TWTs are mostly based on helix slow wave structures (SWSs). However, above 60 GHz, helix SWSs are either very expensive or unfeasible to fabricate due to manufacture limitations. The need of alternative SWSs feasible at millimeter waves has stimulated the investigation of new full-metal SWSs such as the folded waveguide or the double corrugated waveguide [4], [5].

A different family of SWSs, the meander lines, has also shown promising performance suitable for millimeter-wave space TWTs. Meander line SWSs have some advantages in comparison with full-metal structures such as low-cost

production, lower operation voltage and higher interaction impedance [6].

The interaction impedance of a SWS determines how efficient is the exchange of energy between the RF signal and the electron beam. In space applications, both beam voltage and interaction impedance are important design parameters for saving power and reducing the TWT weight, which has direct implications for the final system and launch costs per satellite [7]. A high interaction impedance ($> 3 \Omega$) is obtained by an enhanced axial electric field intensity and more efficient energy exchange between the RF signal and the electron beam. This increases the gain per period of the SWS and permits to reduce the SWS length to produce more compact and lightweight TWTs. A low beam voltage (< 10 kV) allows to use lightweight and compact high voltage power suppliers with substantial payload reduction.

Despite the interest on meander lines, most of the results in literature are simulations, with experimental validation limited to S-parameters. The interaction impedance is usually derived by 3D electromagnetic simulations. An experimental validation is still missing, but it would be of great importance for a more accurate characterization of meander line SWSs.

The phase velocity and the interaction impedance of helix SWSs can be determined, for instance, by solving the field equations [8] or using resonant or non-resonant perturbation methods [9], [10].

This work aims to provide an experimental procedure to determine the phase velocity and, for the first time, the interaction impedance of meander line SWSs.

The experimental validation of the phase velocity is based on the measurement of the phase difference between the same meander line with two different lengths. This method, already proven to give excellent results applied to metal SWSs [11] and meander line SWSs [12], has been extended, for the first time, to Ka-band meander line SWSs.

The second novelty of this work is the development of a theory to experimentally determine the interaction impedance. A perturbation method, similar to the one presented in [9] for helix SWSs based on the work from [13], has been applied for the purpose. A rigorous analytical method has been developed to compute the electromagnetic fields of meander lines to determine the interaction impedance from measurements of the phase difference between a perturbed and an unperturbed meander line SWS.

In order to experimentally validate the two approaches for

This work was supported by the European Space Agency (ESA) in the framework of ESA's Network Partnering Initiative, contract no. 4000122038.

J. M. Socuéllamos, R. Letizia and C. Paoloni are with the Engineering Department, Lancaster University, Lancaster, LA1 4YW, U.K. (e-mail: j.socuellamos@lancaster.ac.uk; r.letizia@lancaster.ac.uk; c.paoloni@lancaster.ac.uk)

R. Dionisio is with the European Space Research and Technology Centre, European Space Agency, 2201 AZ Noordwijk, The Netherlands. (e-mail: roberto.dionisio@esa.int)

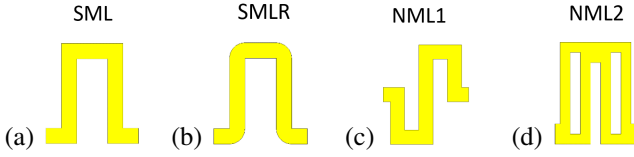


Fig. 1. Single period design of the four meander line topologies studied in this work. SML (a) and SMLR (b) stand for the standard meander line topology with and without round corners and NML1 (c) and NML2 (d) for two novel meander line designs.

measuring both dispersion and interaction impedance, four different meander line topologies have been designed (see Fig. 1) and manufactured at Ka-band. Two novel meander lines (NML1 and NML2) are proposed to improve specific performance depending on the application of the TWT. One, NML1, offers flatter dispersion over a wide band [14], the other, NML2, provides higher interaction impedance but over a narrower band [15]. A standard meander line (SML) (Fig. 1(a)) and the standard meander line with round corners (SMLR) (Fig. 1(b)) are used as reference for comparison with the two novel meander lines, NML1 (Fig. 1(c)) and NML2 (Fig. 1(d)). The experimental results for the phase velocity and the interaction impedance of the four meander line SWSs are discussed and compared with 3D electromagnetic simulations (CST Microwave Studio [16]). Numerical convergence of results in simulations was obtained by modelling the metallization with a local hexahedral mesh with $50 \mu\text{m}^3$ volumetric cells corresponding to one cell every $2 \mu\text{m}$ and $5 \mu\text{m}$ in the vertical and horizontal coordinates, respectively.

II. CALCULATION OF THE PHASE VELOCITY

The phase velocity of a SWS can be experimentally calculated from measurements of the phase difference of two identical SWSs with different lengths (l_1 and l_2) or number of periods (n_1 and n_2). The difference in lengths Δl is a multiple integer $n = n_2 - n_1$ of the pitch length p of the periodic structure, $\Delta l = l_2 - l_1 = np$. The phase delay τ can be defined as the ratio between the variation of phase and frequency $\tau = \Delta\phi/\Delta\omega$. Then, the difference between the phase delay of the SWSs with different lengths is $\Delta\tau = \Delta\phi_2/\Delta\omega - \Delta\phi_1/\Delta\omega$.

The phase velocity $v_p = \Delta l/\Delta\tau$ is, therefore, computed as

$$v_p = \frac{np}{\Delta\phi_2/\Delta\omega - \Delta\phi_1/\Delta\omega}. \quad (1)$$

III. DETERMINATION OF THE INTERACTION IMPEDANCE

A perturbation method is adopted to derive an expression for the interaction impedance K in terms of a measurable quantity such as the propagation constant shift $\Delta\beta$.

The general equation for the calculation of the interaction impedance for the m th transverse and n th axial harmonics at any given point of a particular SWS is given by [17]

$$K_{mn}(x, y, z) = \frac{E_{z,mn}(x, y, z)E_{z,mn}^*(x, y, z)}{2\beta_n^2 P} \quad (2)$$

where $\beta_n = \beta + \frac{2\pi n}{p}$, with β_n being the axial phase constant of the n th space harmonic, β the fundamental axial phase

constant, p the pitch length and m and n integers. $E_{z,mn}$ is the longitudinal electric field magnitude of the n th axial and m th transverse space harmonics, $E_{z,mn}^*$ its complex conjugate and P is the time averaged RF power flow.

When a physical perturbation is introduced in the system under analysis, the propagation constant shift between the perturbed and unperturbed signals can be defined as [13]

$$\Delta\beta_n = \frac{\omega(\epsilon' - \epsilon_2) \int_{\Delta V} \mathbf{E}'_{mn}(x, y, z) \cdot \mathbf{E}^*_{mn}(x, y, z) dV}{4Pp} \quad (3)$$

where \mathbf{E}'_{mn} is the perturbed electric field and \mathbf{E}^*_{mn} is the complex conjugate of the electric field without perturbation. ϵ' and V are the permittivity and the volume of the perturbation, respectively. ϵ_2 is the permittivity of the original medium where the perturbation is applied.

Equation (2) and (3) are valid for any SWS. However, the expressions for the electric fields in these equations need to be derived specifically for the SWS under investigation. In the following, the method will be applied to general meander line SWSs. In particular, expressions for the electromagnetic fields are derived for the four different meander line topologies studied in this work (see Fig. 1). Nevertheless, the procedure permits to obtain the expression of the interaction impedance regardless of the meander line topology.

The model uses a selection of trigonometric functions for computing the electromagnetic fields of meander lines. Even though those functions are considered valid for the purpose, slight differences can be found in literature to describe the fields depending on the approach adopted [18], [19].

The meander line SWS can be assumed made of perfect conductor with infinitesimal thickness placed on a lossless and uniform dielectric substrate. The substrate is surrounded by perfect conductor walls and a ground plane. Following these assumptions, the expressions for the longitudinal components of the electromagnetic field in meander lines can be written as (adapted from [20] for a more general case)

$$E_z(x, y, z) = \sum_{m,n=-\infty}^{\infty} A_{jk,mn} \frac{\sinh(\alpha_{ijk,mn} Y_i)}{\sinh(\alpha_{ijk,mn} B_i)} \sin(k_{jk,m} X_{jk}) e^{-j\beta_n z}, \quad (4)$$

$$H_z(x, y, z) = \sum_{m,n=-\infty}^{\infty} B_{jk,mn} \frac{\cosh(\alpha_{ijk,mn} Y_i)}{\cosh(\alpha_{ijk,mn} B_i)} \cos(k_{jk,m} X_{jk}) e^{-j\beta_n z} \quad (5)$$

where $\alpha_{ijk,mn}^2 = k_{jk,m}^2 + \beta_n^2 - \omega^2 \mu \epsilon_i$.

These expressions contain three indexes i, j and k that vary according to the spatial disposition of the structure and are fundamental to correctly characterize the electromagnetic fields of any meander line topology. Specifically, each index is linked to one spatial dimension; i and k to the transverse vertical and horizontal coordinates, respectively, and j to the longitudinal coordinate.

A standard meander line (SML) enclosed in a rectangular housing, similar to the structure manufactured in this work, is considered as an example to describe the index association.

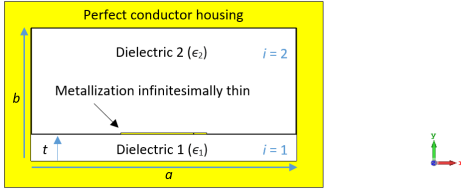


Fig. 2. xy -plane view of the two regions of the meander line to be analyzed. t is the thickness of the substrate, a is the length of the substrate and b is the height of the perfect conductor cavity.

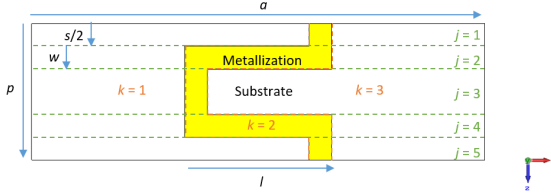


Fig. 3. xz -plane view of the standard meander line. There are five and three regions along the z and x axis, respectively. s is the distance between two consecutive strips, w is the strip width, p is the pitch length, a is the length of the substrate and l is the length of the metallization.

As schematically seen in Fig. 2, the index i (coordinate y) can be either 1 or 2 depending on the region of analysis if the metallization is considered to be infinitesimally thin: the substrate with permittivity ϵ_1 or the medium above with permittivity ϵ_2 . Similarly, the indexes j and k (coordinates z and x , respectively) can be defined taking as a reference the schematic shown in Fig. 3. The index j varies from 1 to 5 in order to consider the five regions with different electromagnetic field. The index k varies from 1 to 3 to define the substrate and metal regions.

As seen in Fig. 2, the expressions for Y_i and B_i in (4) and (5) do not depend on the meander line topology if this is considered infinitesimally thin. However, the other parameters, the field amplitudes A_{jk} and B_{jk} , and X_{jk} and k_{jk} do depend on the meander line shape and vary accordingly.¹

Applying Maxwell's equations to (4) and (5) allows to obtain general expressions for the transverse electric field components as

$$E_x(x, y, x) = \sum_{m,n=-\infty}^{\infty} j \frac{\sinh(\alpha_{ijk,mn} Y_i) \cos(k_{jk,m} X_{jk})}{\beta_n^2 - \omega^2 \mu \epsilon_i} e^{-j\beta_n z} \left(A_{jk,mn} \frac{\partial X_{jk}}{\partial x} \frac{k_{jk,m} \beta_n}{\sinh(\alpha_{ijk,mn} B_i)} + B_{jk,mn} \frac{\partial Y_i}{\partial y} \frac{\alpha_{ijk,mn} \omega \mu}{\cosh(\alpha_{ijk,mn} B_i)} \right), \quad (6)$$

$$E_y(x, y, x) = \sum_{m,n=-\infty}^{\infty} j \frac{\cosh(\alpha_{ijk,mn} Y_i) \sin(k_{jk,m} X_{jk})}{\beta_n^2 - \omega^2 \mu \epsilon_i} e^{-j\beta_n z} \left(A_{jk,mn} \frac{\partial Y_i}{\partial y} \frac{\alpha_{ijk,mn} \beta_n}{\sinh(\alpha_{ijk,mn} B_i)} + B_{jk,mn} \frac{\partial X_{jk}}{\partial x} \frac{k_{jk,m} \omega \mu}{\cosh(\alpha_{ijk,mn} B_i)} \right). \quad (7)$$

Fig. 4 shows the model of a dielectric cylindrical perturbation placed on top of the standard meander line in a similar

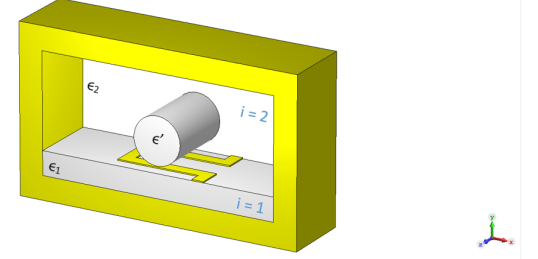


Fig. 4. 3D view of the three regions to be analysed including the perturbation.

configuration to the experimental setup that has been used in this work. The dielectric perturbation with permittivity ϵ' is placed in the region $i = 2$. Three regions are defined: the region within the substrate ($i = 1$), the region above the substrate excluding the perturbation ($i = 2$) and the region within the perturbation.

The fields within the perturbed region are changed in such a way that the field amplitudes A_{jk} and B_{jk} , and the propagation constant β_n are shifted to the equivalent parameters A'_{jk} , B'_{jk} and β'_n , respectively. Setting $i = 2$ in Y_i and B_i as the perturbation is placed in this region, the perturbed field components are then expressed as

$$E'_z(x, y, z) = \sum_{m,n=-\infty}^{\infty} A'_{jk,mn} \frac{\sinh(\alpha'_{jk,mn} Y_2)}{\sinh(\alpha'_{jk,mn} B_2)} \sin(k_{jk,m} X_{jk}) e^{-j\beta'_n z}, \quad (8)$$

$$E'_x(x, y, x) = \sum_{m,n=-\infty}^{\infty} j \frac{\sinh(\alpha'_{jk,mn} Y_2) \cos(k_{jk,m} X_{jk})}{\beta_n'^2 - \omega^2 \mu \epsilon'} e^{-j\beta'_n z} \left(A'_{jk,mn} \frac{\partial X_{jk}}{\partial x} \frac{k_{jk,m} \beta'_n}{\sinh(\alpha'_{jk,mn} B_2)} + B'_{jk,mn} \frac{\partial Y_2}{\partial y} \frac{\alpha'_{jk,mn} \omega \mu}{\cosh(\alpha'_{jk,mn} B_2)} \right), \quad (9)$$

$$E'_y(x, y, x) = \sum_{m,n=-\infty}^{\infty} j \frac{\cosh(\alpha'_{jk,mn} Y_2) \sin(k_{jk,m} X_{jk})}{\beta_n'^2 - \omega^2 \mu \epsilon'} e^{-j\beta'_n z} \left(A'_{jk,mn} \frac{\partial Y_2}{\partial y} \frac{\alpha'_{jk,mn} \beta'_n}{\sinh(\alpha'_{jk,mn} B_2)} + B'_{jk,mn} \frac{\partial X_{jk}}{\partial x} \frac{k_{jk,m} \omega \mu}{\cosh(\alpha'_{jk,mn} B_2)} \right). \quad (10)$$

The interaction impedance can be defined at one arbitrary point (x_0, y_0) according to (2) as

$$K_{mn}(x_0, y_0) = \frac{E_{z,mn}(x_0, y_0) E_{z,mn}^*(x_0, y_0)}{2\beta_n'^2 P}. \quad (11)$$

To relate the interaction impedance at this particular point $K_{mn}(x_0, y_0)$ with the measurable quantity $\Delta\beta_n$, it is necessary to find the relation between the product of fields from (11) with that from (3).

The approach to find this relation is based on the application of interface conditions, first, between the dielectric perturbation and its surrounding medium ($i = 2$), and second, between the meander line substrate ($i = 1$) and the medium over it ($i = 2$). For the first case, the perturbation is assumed to be

¹Expressions for Y_i , B_i , X_{jk} and k_{jk} are derived in App. A for the standard meander line topology (SML) as an example.

uniform along the axial direction. Therefore, the continuity of the tangential \mathbf{E}_t and normal \mathbf{D}_n field components used to relate the perturbed and unperturbed axial field components is valid at any point of the perturbation surface and independent of the z coordinate. Similarly for the second case, at the interface between the substrate ($i = 1$) and the medium ($i = 2$), the tangential \mathbf{E}_t and the normal \mathbf{D}_n field components are continuous.

Applying all these conditions, the following relationships between the electric fields can be found

$$\begin{aligned} E'_{z,mn}(x, y, z)E^*_{z,mn}(x, y, z) = \\ E_{z,mn}(x_0, y_0)E^*_{z,mn}(x_0, y_0) \cdot \\ G_{jk,z} \sinh(\alpha'_{jk,mn}Y_2) \sinh(\alpha_{2jk,mn}Y_2) \sin^2(k_{jk,m}X_{jk}), \end{aligned} \quad (12)$$

$$\begin{aligned} E'_{x,mn}(x, y, z)E^*_{x,mn}(x, y, z) = \\ E_{z,mn}(x_0, y_0)E^*_{z,mn}(x_0, y_0) \cdot \\ G_{jk,x} \sinh(\alpha'_{jk,mn}Y_2) \sinh(\alpha_{2jk,mn}Y_2) \cos^2(k_{jk,m}X_{jk}), \end{aligned} \quad (13)$$

$$\begin{aligned} E'_{y,mn}(x, y, z)E^*_{y,mn}(x, y, z) = \\ E_{z,mn}(x_0, y_0)E^*_{z,mn}(x_0, y_0) \cdot \\ G_{jk,y} \cosh(\alpha'_{jk,mn}Y_2) \cosh(\alpha_{2jk,mn}Y_2) \sin^2(k_{jk,m}X_{jk}) \end{aligned} \quad (14)$$

with $G_{jk,z}$, $G_{jk,x}$ and $G_{jk,y}$ being the coefficients that contain the particularities of every interface condition applied.²

Every expression obtained for the product between the perturbed and unperturbed field components (12)-(14) can be then replaced into (3) as

$$\begin{aligned} \Delta\beta_n = \frac{\omega(\epsilon' - \epsilon_2)}{4Pp} E_{z,mn}(x_0, y_0)E^*_{z,mn}(x_0, y_0) \int_{\Delta V} \sum_{j,k} \\ [G_{jk,z} \sinh(\alpha'_{jk,mn}Y_2) \sinh(\alpha_{2jk,mn}Y_2) \sin^2(k_{jk,m}X_{jk}) + \\ G_{jk,x} \sinh(\alpha'_{jk,mn}Y_2) \sinh(\alpha_{2jk,mn}Y_2) \cos^2(k_{jk,m}X_{jk}) + \\ G_{jk,y} \cosh(\alpha'_{jk,mn}Y_2) \cosh(\alpha_{2jk,mn}Y_2) \sin^2(k_{jk,m}X_{jk})] dV. \end{aligned} \quad (15)$$

Finally, solving for the product $E_{z,mn}(x_0, y_0)E^*_{z,mn}(x_0, y_0)$ in (15) and replacing into (11), the interaction impedance at one selected point $K_{mn}(x_0, y_0)$ can be calculated in terms of the measurable quantities β_n and $\Delta\beta_n$ according to

$$K_{mn}(x_0, y_0) = \frac{2p}{\omega(\epsilon' - \epsilon_2)} \frac{\Delta\beta_n}{\beta_n^2} \frac{1}{I_{mn}} \quad (16)$$

where I_{mn} is the numerical result of the integral in (15).

IV. EXPERIMENTAL SETUP

The four meander line SWSs in Fig. 1 have been fabricated with two different number of periods each, $n_1 = 20$ (see Fig. 5) and $n_2 = 40$, in order to be able to measure the phase velocity. The dimensions of the substrate are 21.812 mm x 2.9 mm for the 20-period length and 33.812 mm x 2.9 mm for the 40-period length. The substrate is alumina with relative

²Equation (12) is derived as an example in App. B.

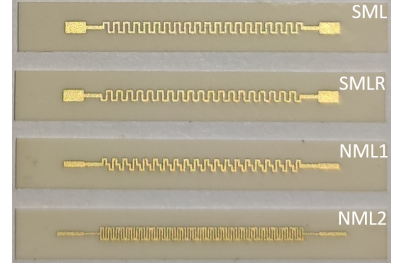


Fig. 5. The four different topologies of the 20-period meander line SWSs manufactured for the experiment.

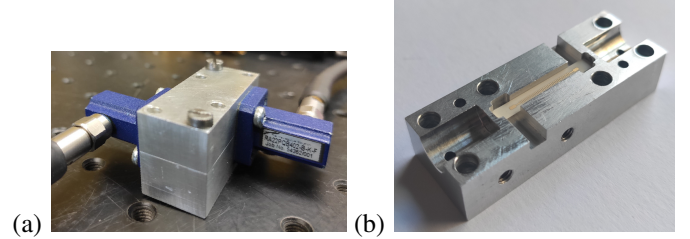


Fig. 6. (a) Measurement setup with the waveguide flanges connected to the housing and (b) bottom half of the housing with one of the meander lines placed inside.

permittivity $\epsilon_1 = 9.9$ and 127 μm thickness. The metallization is made of gold with 10 μm thickness.

Two aluminum housings corresponding to the two different lengths of the meander lines were manufactured. The housings are designed with two WR28 waveguide ports with dimensions 7.112 mm x 3.556 mm, one at each side of the aluminum block, that are connected to the waveguide flanges as seen in the measurement setup in Fig. 6(a). The flanges are then connected to a Vector Network Analyzer to perform the measurements. As shown in Fig. 5, the meander lines are terminated in coupling probes so that the electromagnetic field applied through the waveguide ports can be coupled to the meander line. The final assembly of the meander line inserted into the housing is shown in Fig. 6(b).

The phase velocity measurements for every topology are performed using the same housing and replacing the inner meander line for both 20 and 40-period cases. Then, the phase delay difference is measured for every pair of meander line topologies to obtain the data in (1).

To compute the interaction impedance, the perturbed phase is measured after introducing a nylon ($\epsilon' = 3.4$) rod with radius 120 μm , placed at 450 μm from the metal strip as shown in Fig. 7. The dielectric rod is introduced in the housing by means of two holes that were drilled at both ends of the aluminum holder.

As derived in (16), β and $\Delta\beta$ are the quantities that need to be measured in order to experimentally determine the interaction impedance. The values of β are obtained from the phase velocity measurements as $\beta = \omega/v_p$, and $\Delta\beta$ from the phase difference between the perturbed and unperturbed circuits as $\Delta\beta = \Delta\phi/l$ where l is the length of the circuit.

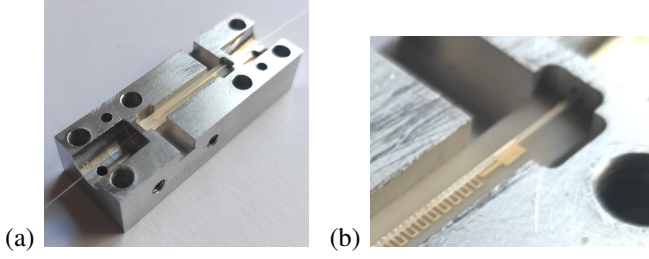


Fig. 7. (a) Bottom half of the housing with the perturbation introduced on top of the meander line. (b) Detail of the perturbation over the meander line.

V. EXPERIMENTAL RESULTS

A. Phase velocity

The measurements of the phase velocity for all the four meander lines are shown in Fig. 8. A measurement error has been added to the results considering that, for a same meander line, different samples were fabricated and measured. In particular, twenty samples were used, two 20-period and 40-period samples of SML and SMLR and three 20-period and 40-period samples of NML1 and NML2. Therefore, to calculate the phase velocity, four curves were computed for SML and SMLR while nine curves were computed for NML1 and NML2. The measurement error, represented by a shadowed area in Fig. 8, is given by the highest and lowest phase velocity measured for the various samples available. The measurement curves, which are drawn with solid lines in Fig. 8, are the mean value of the results obtained from the various samples.

The measurement results for NML1 and NML2 (Fig. 8(c) and 8(d)) show good correlation with the simulated curves. However, the experimental curves for SML and SMLR (Fig. 8(a) and 8(b)) show a correct trend but values slightly higher than the obtained for the simulations at the low-half frequency band. This difference could be due to manufacture tolerances or slight deviations in the position of the meander line inside the housings.

B. Interaction impedance

The experimental curves for the interaction impedance for the four meander lines considered are compared with the simulation results in Fig. 9(a) and 9(b) for SML and SMLR, and Fig. 9(c) and 9(d) for NML1 and NML2. Similar to the measurements of the phase velocity, two samples of SML and SMLR and three samples of NML1 and NML2 have been used for the tests. Therefore, the shadowed areas in Fig. 9, account for the deviation from the mean value considering the different samples of the same meander line. The simulated curves are obtained by two different methods: simulating the equivalent virtual experiment to obtain the data to apply (16) and using the Eigenmode solver in CST-MWS based on (2). The interaction impedance is computed at the centre of the perturbation, corresponding to a distance of $570 \mu\text{m}$ from the metallization ($450 \mu\text{m} + 120 \mu\text{m}$ of the rod radius).

The good agreement between experiment and simulations demonstrates the validity of the method. In meander lines, the longitudinal electric field is concentrated close to the

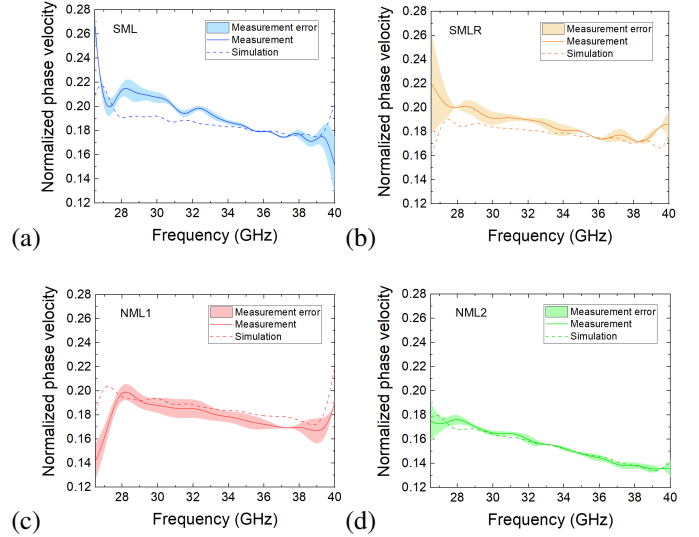


Fig. 8. Comparison of the phase velocity measurements (solid curves plus error) with the simulation curves (dashed curves). (a) SML, (b) SMLR, (c) NML1 and (d) NML2.

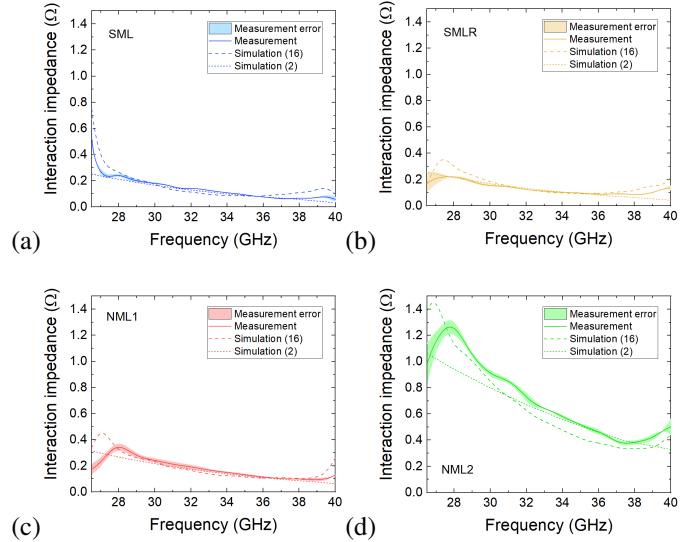


Fig. 9. Comparison of the interaction impedance measurements (solid curves plus error) with the simulation curves using (16) (dashed curves) and using (2) (dotted curves). (a) SML, (b) SMLR, (c) NML1 and (d) NML2.

metallization. Consequently, the interaction impedance grows as the calculation point approaches the meander line. The low interaction impedance measured in Fig. 9 is due to the position of the perturbation far from the metallization. According to simulations, if the perturbation is placed at a distance of $50 \mu\text{m}$ from the metallization, the interaction impedance is over 3Ω for the four meander lines. In future experiments, the perturbation will be placed closer to the meander line to measure higher values of the interaction impedance.

VI. CONCLUSION

The first experimental computation of the phase velocity at Ka-band and a new method for measuring the interaction impedance in meander line SWSS for TWTs have been presented. Four Ka-band meander line SWSS were manufactured

and tested to validate the theory. In general, the experimental results showed good agreement with 3D electromagnetic simulations.

The presented methods are useful experimental tools for design and test of a new family of meander line SWSs for a new generation of low-cost and lightweight space TWTs for millimeter-wave communications. High interaction impedance and low beam voltage are important meander line features to reduce the size and weight of the TWT and the power supply, with benefits on the mission cost for cost-effective satellite communication systems.

APPENDIX A

DERIVATION OF THE PARAMETERS Y_i , B_i , X_{jk} AND k_{jk}

Assuming an infinitesimal thickness for the metallization, the characterization over the transverse vertical component is not dependent on the meander topology. As seen in Fig. 2, the structure is divided in two regions along the y coordinate ($i = 1, 2$). To obtain the values for Y_i and B_i , these two regions need to satisfy the boundary conditions of the structure, $E_z = 0$ at $y = 0$ and $y = b$. Therefore, expressions for the axial component of the electric field can be obtained depending on the region of analysis as

$0 < y < t$ or $i = 1$

$$E_z(x, y, z) = \sum_{m,n=-\infty}^{\infty} A_{jk,mn} \frac{\sinh(\alpha_{1jk,mn} Y_1)}{\sinh(\alpha_{1jk,mn} B_1)} \sin(k_{jk,m} X_{jk}) e^{-j\beta_n z}$$

with $Y_1 = y$ and $B_1 = t$.

$t < y < b$ or $i = 2$

$$E_z(x, y, z) = \sum_{m,n=-\infty}^{\infty} A_{jk,mn} \frac{\sinh(\alpha_{2jk,mn} Y_2)}{\sinh(\alpha_{2jk,mn} B_2)} \sin(k_{jk,m} X_{jk}) e^{-j\beta_n z}$$

with $Y_2 = b - y$ and $B_2 = b - t$.

The study over the x and z coordinates depends on the particular topology of the meander line. The longitudinal electric field expressions for the standard meander line are derived according to Fig. 3. Five regions can be defined along the z coordinate, $j = 1, 2, 3, 4, 5$, and three regions over the x coordinate, $k = 1, 2, 3$. The regions $k = 1$ and $k = 3$ refer to the left and right hand side of the substrate, respectively, whereas $k = 2$ is the region containing the metallization. Therefore, the limits for the regions along the x coordinate are not fixed and depend on the z position of analysis. For the case of SML, the fields in regions $j = 1$ and $j = 5$ are the same and also those in regions $j = 2$ and $j = 4$. In order to derive expressions for the parameters X_{jk} and k_{jk} , boundary conditions of the structure are applied. Specifically, $E_z = 0$ at $x = 0$ and $x = a$ and also at the areas where the metallization is located. These expressions can be then determined as

$0 < z < s/2, 3s/2 + 2w < z < p$ and $0 < x < a/2 + l/2 - w$ or $j = 1, 5$ and $k = 1$

$$E_z(x, y, z) = \sum_{m,n=-\infty}^{\infty} A_{11,mn} \frac{\sinh(\alpha_{i11,mn} Y_i)}{\sinh(\alpha_{i11,mn} B_i)} \sin(k_{11,m} X_{11}) e^{-j\beta_n z}$$

with $k_{11,m} = \frac{(2m-1)\pi}{a/2+l/2-w}$ and $X_{11} = x$.

$0 < z < s/2, 3s/2 + 2w < z < p$ and $a/2 + l/2 - w < x < a/2 + l/2$ or $j = 1, 5$ and $k = 2$

$$E_z(x, y, z) = 0$$

$0 < z < s/2, 3s/2 + 2w < z < p$ and $a/2 + l/2 < x < a$ or $j = 1, 5$ and $k = 3$

$$E_z(x, y, z) = \sum_{m,n=-\infty}^{\infty} A_{13,mn} \frac{\sinh(\alpha_{i13,mn} Y_i)}{\sinh(\alpha_{i13,mn} B_i)} \sin(k_{13,m} X_{13}) e^{-j\beta_n z}$$

with $k_{13,m} = \frac{(2m-1)\pi}{a/2-l/2}$ and $X_{13} = a - x$.

$s/2 < z < s/2 + w, 3s/2 + w < z < 3s/2 + 2w$ and $0 < x < a/2 - l/2$ or $j = 2, 4$ and $k = 1$

$$E_z(x, y, z) = \sum_{m,n=-\infty}^{\infty} A_{21,mn} \frac{\sinh(\alpha_{i21,mn} Y_i)}{\sinh(\alpha_{i21,mn} B_i)} \sin(k_{21,m} X_{21}) e^{-j\beta_n z}$$

with $k_{21,m} = \frac{(2m-1)\pi}{a/2-l/2}$ and $X_{21} = x$.

$s/2 < z < s/2 + w, 3s/2 + w < z < 3s/2 + 2w$ and $a/2 - l/2 < x < a/2 + l/2$ or $j = 2, 4$ and $k = 2$

$$E_z(x, y, z) = 0$$

$s/2 < z < s/2 + w, 3s/2 + w < z < 3s/2 + 2w$ and $a/2 + l/2 < x < a$ or $j = 2, 4$ and $k = 3$

$$E_z(x, y, z) = \sum_{m,n=-\infty}^{\infty} A_{23,mn} \frac{\sinh(\alpha_{i23,mn} Y_i)}{\sinh(\alpha_{i23,mn} B_i)} \sin(k_{23,m} X_{23}) e^{-j\beta_n z}$$

with $k_{23,m} = \frac{(2m-1)\pi}{a/2-l/2}$ and $X_{23} = a - x$.

$s/2 + w < z < 3s/2 + w$ and $0 < x < a/2 - l/2$ or $j = 3$ and $k = 1$

$$E_z(x, y, z) = \sum_{m,n=-\infty}^{\infty} A_{31,mn} \frac{\sinh(\alpha_{i31,mn} Y_i)}{\sinh(\alpha_{i31,mn} B_i)} \sin(k_{31,m} X_{31}) e^{-j\beta_n z}$$

with $k_{31,m} = \frac{(2m-1)\pi}{a/2-l/2}$ and $X_{31} = x$.

$s/2 + w < z < 3s/2 + w$ and $a/2 - l/2 < x < a/2 - l/2 + w$ or $j = 3$ and $k = 2$

$$E_z(x, y, z) = 0$$

$s/2 + w < z < 3s/2 + w$ and $a/2 - l/2 + w < x < a$ or $j = 3$ and $k = 3$

$$E_z(x, y, z) = \sum_{m,n=-\infty}^{\infty} A_{33,mn} \frac{\sinh(\alpha_{i33,mn} Y_i)}{\sinh(\alpha_{i33,mn} B_i)} \sin(k_{33,m} X_{33}) e^{-j\beta_n z}$$

with $k_{33,m} = \frac{(2m-1)\pi}{a/2+l/2-w}$ and $X_{33} = a - x$.

APPENDIX B DERIVATION OF (12)

The product between the axial components of the perturbed and the complex unperturbed fields, (8) and the conjugate equivalent of (4), can be written as

$$E'_{z,mn}(x, y, z) E_{z,mn}^*(x, y, z) = \frac{A'_{jk,mn}}{A_{jk,mn}} A_{jk,mn}^* A_{jk,mn} \frac{\sinh(\alpha'_{jk,mn} Y_2) \sinh(\alpha_{ijk,mn} Y_i)}{\sinh(\alpha'_{jk,mn} B_2) \sinh(\alpha_{ijk,mn} B_i)} \sin^2(k_{jk,m} X_{jk}) e^{-j(\beta'_n - \beta_n)z}. \quad (17)$$

The unperturbed axial field component at one given point (x_0, y_0) within the region of perturbation is defined, according to (4), as

$$E_{z,mn}(x_0, y_0, z) = A_{jk,mn} \frac{\sinh(\alpha_{2jk,mn} Y_2^0)}{\sinh(\alpha_{2jk,mn} B_2)} \sin(k_{jk,m} X_{jk}^0) e^{-j\beta_n z}, \quad (18)$$

and multiplying with its complex conjugate gives

$$E_{z,mn}(x_0, y_0) E_{z,mn}^*(x_0, y_0) = A_{jk,mn} A_{jk,mn}^* \frac{\sinh^2(\alpha_{2jk,mn} Y_2^0)}{\sinh^2(\alpha_{2jk,mn} B_2)} \sin^2(k_{jk,m} X_{jk}^0). \quad (19)$$

Solving for the product between the field amplitudes gives

$$A_{jk,mn} A_{jk,mn}^* = \frac{E_{z,mn}(x_0, y_0) E_{z,mn}^*(x_0, y_0)}{\frac{\sinh^2(\alpha_{2jk,mn} Y_2^0)}{\sinh^2(\alpha_{2jk,mn} B_2)} \sin^2(k_{jk,m} X_{jk}^0)}. \quad (20)$$

The continuity of the tangential axial field component at the perturbation surface implies that at one given point (x_1, y_1) of the surface, $E'_z(x_1, y_1, z) = E_z(x_1, y_1, z)$. By using this relation, a relationship between the unperturbed and perturbed field coefficients can be found

$$\frac{A'_{jk,mn}}{A_{jk,mn}} e^{-j(\beta'_n - \beta_n)z} = \frac{\sinh(\alpha_{2jk,mn} Y_2^1) \sinh(\alpha'_{jk,mn} B_2)}{\sinh(\alpha'_{jk,mn} Y_2^1) \sinh(\alpha_{2jk,mn} B_2)}. \quad (21)$$

Finally, replacing the expressions from (20) and (21) into (17), the product of the perturbed and unperturbed fields can be rewritten in terms of the product between the original and complex unperturbed axial field components as

$$E'_{z,mn}(x, y, z) E_{z,mn}^*(x, y, z) = E_{z,mn}(x_0, y_0) E_{z,mn}^*(x_0, y_0) G_{jk,z} \sinh(\alpha'_{jk,mn} Y_2) \sinh(\alpha_{2jk,mn} Y_2) \sin^2(k_{jk,m} X_{jk}), \quad (22)$$

with

$$G_{jk,z} = \frac{\sinh(\alpha_{2jk,mn} Y_2^1)}{\sinh(\alpha'_{jk,mn} Y_2^1) \sinh^2(\alpha_{2jk,mn} Y_2^0) \sin^2(k_{jk,m} X_{jk}^0)}.$$

Equation (13) and (14) can be derived in a similar fashion applying the interface conditions that correspond to each field component.

REFERENCES

- [1] G. Giambene, S. Kota and P. Pillai, "Satellite-5G Integration: A Network Perspective", *IEEE New.*, Vol. 32, No. 5, pp. 25-31, Sep./Oct. 2018.
- [2] A. I. Perez-Neira, M. A. Vazquez, M. R. Bhavani Shankar, S. Maleki and S. Chatzinotas, "Signal Processing for High-Throughput Satellites: Challenges in New Interference-Limited Scenarios", *IEEE Signal Process. Mag.*, Vol. 36, No. 4, pp. 112-131, Jul. 2019.
- [3] N. Ayllon, P. Angeletti, M. Ludwig and R. Dionisio, "An overview of European Spaceborne Vacuum Tube Amplifiers and System Needs", in *Proc. 18th Int. Vac. Electron. Conf.*, London, UK, Apr. 2017.
- [4] C. W. Robertson, A. W. Cross, C. Gilmour, D. Dyson, P. G. Huggard, F. Cahill, M. Beardsley, R. Dionisio and K. Ronald, "71-76 GHz Folded Waveguide TWT for Satellite Communications", in *Proc. 20th Int. Vac. Electron. Conf.*, Busan, South Korea, Apr. 2019.
- [5] X. Li, X. Huang, S. Mathisen, R. Letizia and C. Paoloni, "Design of 71-76 GHz Double-Corrugated Waveguide Traveling-Wave Tube for Satellite Downlink", *IEEE Trans. Electron Devices*, Vol. 65, No. 6, pp. 2195-2200, Jun. 2018.
- [6] G. Ullisse, V. Krozer, N. Ryskin, A. Starodubov, A. Serdobintsev, A. Pavlov, V. Galushka and M. Samarskiy, "Fabrication and Measurements of a Planar Slow Wave Structure Operating in V-band", in *Proc. 20th Int. Vac. Electron. Conf.*, Busan, South Korea, Apr. 2019.
- [7] G. Kornfeld and E. Bosch, "From History to Future of Satellite TWT Amplifiers", *Frequenz*, Vol. 55, No. 9-10, pp. 258-262, Sep. 2001.
- [8] S. D'Agostino, F. Emma and C. Paoloni, "Accurate Analysis of Helix Slow-Wave Structures", *IEEE Trans. Electron Devices*, Vol. 45, No. 7, pp. 1605-1613, Jul. 1998.
- [9] C. L. Kory and J. A. Dayton, "Computational Investigation of Experimental Interaction Impedance Obtained by Perturbation for Helical Traveling-Wave Tube Structures", *IEEE Trans. Electron Devices*, Vol. 45, No. 9, pp. 2063-2071, Dec. 1998.
- [10] S. J. Rao, S. Ghosh, P. K. Jain and B. N. Basu, "Nonresonant Perturbation Measurements on Dispersion and Interaction Impedance Characteristics of Helical Slow-Wave Structures", *IEEE Trans. Microw. Theory Techn.*, Vol. 45, No. 9, pp. 1585-1593, Sep. 1997.
- [11] C. Paoloni, M. Mineo, M. Henry and P. G. Huggard, "Double Corrugated Waveguide for Ka-band Traveling Wave Tube", *IEEE Trans. Electron Devices*, Vol. 62, No. 11, pp. 3851-3856, Nov. 2015.
- [12] C. Chua and S. Aditya, "A 3-D U-Shaped Meander-Line Slow-Wave Structure for Traveling-Wave-tube Applications", *IEEE Trans. Electron Devices*, Vol. 60, No. 3, pp. 1251-1256, Mar. 2013.
- [13] R. P. Lagerstrom, "Interaction impedance measurements by perturbation of traveling waves", Tech. Rep. no. 7, Stanford Electronics Laboratories, Stanford Univ., Stanford, CA, USA, Feb. 1957.
- [14] J. M. Socu llamos, R. Letizia, R. Dionisio and C. Paoloni, "Large Signal Analysis of a New Meander Line Topology for W-band TWTs", in *Proc. 12th UK/Europe-China Workshop mm-Wav., THz Tech.*, London, UK, Aug. 2019.
- [15] J. M. Socu llamos, R. Letizia, R. Dionisio and C. Paoloni, "Novel Meander Line Slow Wave Structure for W-band TWT", in *Proc. 45th Int. Conf. Infrared, mm., THz-Wav.*, virtual, Nov. 2020.
- [16] CST-MWS. [Online]. Available: <https://www.cst.com/products/csts2>
- [17] A. S. Gilmour, "Principles of Traveling Wave Tubes", Artech House Radar Library, Michigan Univ., Boston, MA, USA, Dec. 1994.
- [18] T. Itoh and R. Mittra, "Spectral-Domain Approach for Calculating the Dispersion Characteristics of Microstrip Lines", *IEEE Trans. Microw. Theory Techn.*, Vol. 21, No. 7, pp. 496-499, Jul. 1973.
- [19] J. A. Weiss, "Dispersion and Field Analysis of a Microstrip Meander-Line Slow-Wave Structure", *IEEE Trans. Microw. Theory Techn.*, Vol. 22, No. 12, pp. 1194-1201, Dec. 1974.
- [20] D. G. Zhang, Edward K. N. Yung and H. Y. Ding, "Dispersion characteristics of a novel shielded periodic meander line", *Microw. Opt. Techn. Lett.*, Vol. 12, No. 1, pp. 1-5, May 1996.